

PERSPECTIVE • OPEN ACCESS

## Advancements and challenges in strained group-IV-based optoelectronic materials stressed by ion beam treatment

To cite this article: Mateus G Masteghin *et al* 2024 *J. Phys.: Condens. Matter* **36** 431501

View the [article online](#) for updates and enhancements.







You may also like

- [A next-generation liquid xenon observatory for dark matter and neutrino physics](#)  
J Aalbers, S S AbdusSalam, K Abe et al.
- [Black holes, gravitational waves and fundamental physics: a roadmap](#)  
Abbas Askar, Chris Belczynski, Gianfranco Bertone et al.
- [2021 roadmap on lithium sulfur batteries](#)  
James B Robinson, Kai Xi, R Vasant Kumar et al.



## Perspective

# Advancements and challenges in strained group-IV-based optoelectronic materials stressed by ion beam treatment

Mateus G Masteghin<sup>1,\*</sup> ,  
Benedict N Murdin<sup>1</sup> ,  
Dominic A Duffy<sup>1,2,3</sup> ,  
Steven K Clowes<sup>1</sup> ,  
David C Cox<sup>1</sup> ,  
Stephen J Sweeney<sup>1,2,3</sup> ,  
and Roger P Webb<sup>4</sup> 

<sup>1</sup> Advanced Technology Institute,  
University of Surrey, Guildford GU2  
7XH, United Kingdom

<sup>2</sup> James Watt School of Engineering,  
University of Glasgow, Glasgow G12  
8LT, United Kingdom

<sup>3</sup> ZiNIR Ltd, Eastbourne, United  
Kingdom

<sup>4</sup> Ion Beam Centre, University of  
Surrey, Guildford GU2 7XH, United  
Kingdom

E-mail:

[m.galluccimasteghin@surrey.ac.uk](mailto:m.galluccimasteghin@surrey.ac.uk)

## Abstract

In this perspective article, we discuss the application of ion implantation to manipulate strain (by either neutralizing or inducing compressive or tensile states) in suspended thin films. Emphasizing the pressing need for a high-mobility silicon-compatible transistor or a direct bandgap group-IV semiconductor that is compatible with complementary metal–oxide–semiconductor technology, we underscore the distinctive features of different methods of ion beam-induced alteration of material morphology. The article examines the precautions needed during experimental procedures and data analysis and explores routes for potential scalable adoption by the semiconductor industry. Finally, we briefly discuss how this highly controllable strain-inducing technique can facilitate enhanced manipulation of impurity-based spin quantum bits (qubits).

Keywords: ion implantation, tensile strain, direct bandgap semiconductors, quantum technology

## 1. Overview of the effect of strain in group-IV semiconductors

The impact of microelectronics in society has been transformative, primarily attributable to the advancements in miniaturized metal–oxide–semiconductor field-effect transistors (MOSFETs) and silicon-based complementary metal–oxide–semiconductor (CMOS) technologies [1]. Meanwhile, photonics is dominated by more expensive III–V materials, except for passive photonic devices, such as waveguides, modulators, and switches. These have been increasingly successful due to the advantages of integrating photonic properties with lower-cost mass-production benefits via well-established electronic devices [1, 2].

Despite the success of silicon (Si) in electronics, an efficient Si-based light emitter allowing full integration of photonics and electronics remains elusive, due to the well-known fundamental physical limitation of Si owing to its indirect bandgap. This makes Si a weak light emitter since phonons are required for indirect radiative transitions to conserve energy and momentum, and in the language of quantum mechanics, the matrix element that determines the probability of the process is the product of two small terms for the photon and the phonon steps and has overall very low cross-section. Other non-radiative

\* Author to whom any correspondence should be addressed.



Original content from this work may be used under the terms of the [Creative Commons Attribution 4.0 licence](https://creativecommons.org/licenses/by/4.0/). Any further distribution of this work must maintain attribution to the author(s) and the title of the work, journal citation and DOI.

processes dominate, such as the Auger effect where energy and momentum of an electron-hole recombination are taken up by excitation of a third charge carrier, which reduces the efficiency of Si optical emitters. As the radiative recombination lifetime for direct transitions (on the order of nanoseconds) is orders of magnitude shorter than for indirect transitions (microseconds or milliseconds), for the same quantum yield a direct semiconductor will emit up to a million times more photons per second than an indirect semiconductor, leading to direct bandgap III–V materials dominating active photonics. Given the many benefits in cost, processing, and sustainability offered by the prospect of silicon integration, this has spurred a search for alternative approaches to integrating direct light sources on silicon. These can be broken into three approaches; (1) the hybrid integration of active III–V materials and devices on silicon (e.g. chip/wafer bonding/fusion) [3], (2) the development of monolithic integration of III–V light sources on silicon, most notably the use of quantum dots [4, 5], or (3) through manipulation of silicon itself, for example through the use of alloys such as GeSn [6], using high tensile strain [7] and/or high amounts of n-type doping [8]. Approaches (1) and (2) provide the advantage of relatively high wall-plug efficiency devices being achievable at the key data and telecoms wavelengths of 1310 nm [5] and 1550 nm [9]. However, particularly in the case of (1), scalability and yield are challenging. Approach (2) using quantum dot-based active regions is presently limited to 1310 nm operation. Approach (3) is in many ways preferable owing to the simpler route to CMOS compatibility using group-IV materials. However, both the use of high tensile strain and alloying inevitably lead to operation at longer wavelengths which limits their applications in optical communications. Despite this, they do provide an opportunity to develop sensors in the mid-infrared. In the remainder of this paper, we focus on the strain engineering route in group-IV semiconductors.

The incorporation of strain into the crystal lattice significantly influences semiconductor band structure by both modifying the spacing of the periodic unit cell potential and breaking crystal symmetry. For a given biaxial strain in the plane of the layer, elasticity theory describes the corresponding tetragonal distortion (and so perpendicular strain  $\varepsilon_{\perp}$ ) based on the elastic tensor of the material. When applying biaxial strain, the unit cell distortions modify the bulk band edges in a manner that can be described by the deformation potential theory [10] and divided into two contributions: hydrostatic deformation (which preserves the symmetry of the unit cell) and shear deformation (which preserves the volume of the unit cell). In the case of [001] tensile strain in silicon and germanium (Ge), this results in a decrease in the conduction band minima at both the  $\Gamma$ - and L-valleys, an increase (and splitting) in the six-fold degenerate  $\Delta$ -valley conduction band minima, and a splitting of the valence band (VB) into light-hole (LH) and heavy-hole (HH) bands at the center of the Brillouin zone ( $\Gamma$ ). As each of the conduction band valleys shifts with strain at different rates, for sufficient tensile strain an indirect-to-direct bandgap crossover can occur.

For bulk silicon, biaxial tensile strains between 10%–13% (and >13% uniaxial strain) are required for conversion into a direct bandgap semiconductor [11]. Although introducing such strain levels to bulk Si via epitaxy growth is very difficult to achieve, smaller amounts have been demonstrated to improve the light emission efficiency. On the other hand, a combined effect of reduced dimensions (quantum confinement) and tensile strain permits an indirect-to-direct transition at much lower tensile strain levels due to an overall downshift of the conduction band, in addition to resonantly enhanced luminescence. The intricate interplay between quantum confinement and tensile strain can be explored when adopting 1D or 2D structures in which this transition was observed for Si nanocrystals under 4% tensile load [12]. Alternatively, an interesting and potentially useful avenue to explore is anisotropy in the crystal structure, and hence the band structure, of silicon. Band structure calculations for different uniaxial loads in

[100], [110], and [111] directions of a silicon nanowire ( $\sim 100$  nm diameter) predict an indirect-to-direct transition at 4% load along [110] direction and 14% load along [111] direction [13].

There are several other benefits of strain in semiconductor device engineering, as discussed in Sweeney *et al* [14]. For example, limits on semiconductor transistor miniaturization occur due to heat generation [15–17] which researchers are trying to minimize through the engineering of the effective mass in III–V high-electron-mobility-transistors (HEMTs), e.g. based on gallium arsenide (GaAs) [18]. However, such an approach to HEMTs is not yet ready for mass production, nor currently truly CMOS-compatible. Therefore, strained silicon devices could offer an alternative to III–V HEMTs that are compatible with existing industry processes. For example, the mobility of Si nMOSFETs under just 1% tensile strain is increased by up to 15% and even up to 40% in Si thin film transistors under  $\sim 0.6\%$  strain [19, 20]. These benefits arise because silicon has six-fold ( $\Delta_6$ ) conduction band degeneracy, and under the uniaxial strain along a [100] or [110] direction (or biaxial strain in a plane perpendicular to these directions) this splits into a two-fold ( $\Delta_2$ ) and a four-fold ( $\Delta_4$ ) set. The energy gap between  $\Delta_2$  and  $\Delta_4$  increases with strain [21, 22] and the Fermi energy settles into the lower of the two sets (depending on the sign of the strain), which causes a reduction in electron scattering in n-type simply because of the reduction in available final states for scattering at the Fermi energy. This increases mobility and, consequently, decreases noise and heating effects. Moreover, the strain also splits the LH and HH VBs, further reducing scattering in p-type silicon.

Germanium, another group-IV element, can be grown on Si and silicon-on-insulator (SOI) substrates, exhibiting superior properties to Si in several respects due to its significantly smaller indirect-direct bandgap splitting energy. This leads to an indirect-to-direct bandgap conversion at a much lower strain compared to Si. The exact strain required for the indirect-to-direct transition depends on sample specifics such as dimensionality (e.g. 2D or bulk) and temperature. For example, a threshold of 2.0% biaxial strain has been estimated (figure 1), based on model-solid theory calculations following the approach of Krijn [23] using deformation and bandgap parameterizations from [24]. Therefore, numerous attempts have been made to achieve a direct bandgap in Ge, including alloying Ge with metallic tin (Sn) [25] driven by band-mixing effects [26], or more successfully, applying tensile strain combined with high levels of n-type doping [27].

Although strained or alloy-engineered Ge has shown some success, the high doping levels required for lasing and the consequent high quasi-Fermi level imply that merely reaching the threshold for indirect-to-direct bandgap is insufficient. Higher strain levels are necessary to counteract loss processes such as free-carrier absorption and Auger recombination. Consequently, the lasers produced thus far are inefficient, requiring prohibitive high-power levels to reach the lasing threshold, rendering them unsuitable for practical applications. Achieving a direct bandgap Si-compatible semiconductor with a narrower bandgap would lead to longer wavelengths in the mid-infrared, which is rich with applications due to the high density of fundamental molecular absorption lines (fingerprints) [28]. Consequently, there are numerous applications for chemical sensing such as in environmental monitoring and for early diagnosis of disease from exhaled breath, that would benefit from the availability of cheaper but also more efficient photonic devices operating at these wavelengths.

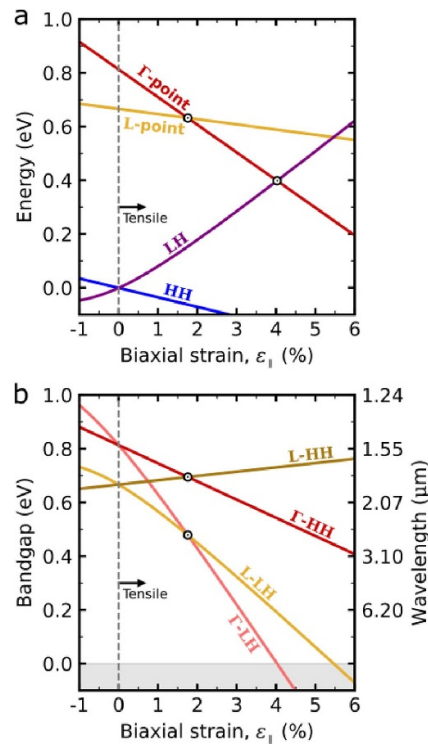


**Figure 1.** Calculated bulk [001] germanium following the approach of Krijn [23], giving (a) band edge energies and (b) bandgap as a function of biaxial tensile strain  $\epsilon_{||}$ , showing the emergence of a direct bandgap in the mid-infrared range. The filled markers indicate strains at which an indirect-to-direct transition occurs (first,  $\epsilon_{||} \approx 2\%$ ) and then where a zero-energy bandgap is reached (second,  $\epsilon_{||} \approx 4\%$ ).

## 2. Strained group-IV semiconductors: historical perspective

### 2.1. Challenges when straining semiconductors at the large scale

Integrating strained group-IV materials with traditional CMOS technology can be achieved via the epitaxial growth of a Si layer on a Ge substrate (or vice-versa). In such a system, the strain is produced through the alignment of the Si atoms with the Ge atoms to compensate for the mismatch between the Si (5.431 Å) and Ge (5.658 Å) lattices. The epitaxial process is semiconductor industry-ready and allows the generation of reproducible results at the wafer scale. Primarily, epitaxial growth aims to reduce strain rather than exacerbate it. During deposition of a strained layer, if the layer thickness exceeds a given critical thickness, lattice mismatch and differences in thermal expansion coefficients can lead to relaxation through the formation of a three-dimensional island or the generation of misfit dislocations [29, 30]. These defect centers serve as active nonradiative recombination sites, thereby diminishing device performance by raising the laser threshold [31]. Similarly, Si epitaxy on silicon dioxide ( $\text{SiO}_2$ ) also induces strain, contingent upon temperature and/or annealing times. In this case, in contrast to a lattice mismatch-induced strain, this phenomenon arises from disparities in thermal expansion coefficients, wherein the Si experiences greater contraction during the cooling phase [32]. Although Si/Ge and other group-IV interfaces may accommodate strains of up to 4.2%, and the growth of group-IV materials on buffer layers holds promise for similar strains, attaining a device with such strain levels while maintaining low defect rates remains a challenge [33].

An alternative to overcome this intrinsic limitation is to start from a low-strain relatively defect-free substrate and add steps in order to enhance the strain at the active area of the device. The most successful technique was dubbed ‘smart-cuts’

and consists of introducing stress concentration at the curvature of the cuts (or cuts edges), achieved through precise lithography and reactive ion etching processes [34]. Despite employing multiple lithography steps, reported strains are generally limited to below 2%. Notably, in the case of undercut silicon nanowires, strains of up to 4.5% have been successfully achieved [35]. In the realm of Ge-suspended micro-bridges, uniaxial strains as high as 5.9% have been achieved, with lasing observed to occur at strains exceeding 5.4% at a temperature of 20 K [7]. While these methods prove effective in overcoming certain limitations and enhancing the performance of optoelectronic devices, it is crucial to note that the resultant strain is predominantly dictated by the residual stresses present in the wafer at the initiation of the process. The capacity for fine-tuning this strain is consequently limited with an upper threshold. Hence, there is a continued search for an alternative method capable of deterministically inducing strain, ideally within an active layer with minute defect density.

## 2.2. Effects of ion–matter interaction

One way to modify material properties by the introduction, dislodgement, or removal of atoms is via ion implantation. During implantation, energy transfer between the primary ions and the substrate atoms occurs through two distinct mechanisms: nuclear and electronic energy losses; following elastic collisions with the atoms' nuclei or interactions between the charged ions and bound electrons, respectively. Hence, the type (species and valency) and energy of the ions, the atomic number and density of the substrate material, and these two energy loss mechanisms will determine the ability of the material to slow down and eventually stop the energetic ions as they penetrate the substrate [36]. Understanding these parameters is crucial for controlling the implantation process, as they determine the penetration depth and spatial distribution of the damage. The stopping and range of ions in matter [37] calculations show that nuclear energy loss dominates at lower energies (below  $10^4$  keV) while electronic losses become more important at higher implantation energies. This is significant because when nuclear losses predominate, a substantial number of lattice ions displacements occur, leading to the introduction of lattice defects or changes in the sample morphology [36, 38]. In contrast, electron energy loss typically results in a lower density of induced defects along the ion's path, although highly energetic swift heavy [39] or highly charged ions [40] can still lead to significant defect creation.

It was observed that exposure of thin (200 nm) silicon nitride ( $\text{Si}_3\text{N}_4$ ) cantilevers to a 50 keV  $\text{Ga}^+$  beam at low doses ( $<48 \times 10^{15}$  ions  $\text{cm}^{-2}$ ) resulted in surface swelling, while higher doses led to depletion as atoms were sputtered [41]. Kim *et al* [41] attributed this out-of-plane swelling to a thermal spike followed by an in-plane thermal expansion that causes the ion-irradiated region to laterally expand, i.e. an elongation of its dimensions parallel to the sample surface. Accordingly, the material shrinks in the direction perpendicular to the surface (along the ion irradiation direction) due to the Poisson's ratio [42]. This in-plane biaxial expansion causes the cantilever to bow in the irradiated area to accommodate for the strain. A similar morphology-changing effect, described as 'ion-beam hammering' [43, 44], was also observed for other amorphous materials (as well as thermally insulators, e.g.  $\text{SiO}_2$  [43] and  $\text{Si}_3\text{N}_4$  [41]) under high-energy (in the order of MeV) irradiation. This effect takes place when the ion beam range is larger than the sample thickness and the average electronic energy loss is higher than the  $0.60 \text{ keV nm}^{-1}$  threshold [43, 44]. Kim *et al* [41] suggested that even at energies below this threshold, where nuclear stopping predominates and ions undergo frequent elastic nuclear scattering, on average the ion track maintains some directionality and the mechanism described above may still dominate changes in the morphology. This same out-of-plane swelling was also reported for

30 keV Ga<sup>+</sup> [45] or 60 keV Si<sup>++</sup> [46] implants into bulk Si (a good thermal dissipator), suggesting other mechanisms are also involved in ion-induced swelling, being the former attributed to Ga accumulation at small doses and the latter ascribed to amorphization expansion in the plane followed by outward bowing. Another example to support the miscellaneous reports is when 30 keV Ga<sup>+</sup> irradiates a gold (Au) thin film [47] in which Au atoms sputtered/coalesce and the replacement of larger Au atoms by Ga causes a contraction on the top layer (delimited by the implantation depth, 7.6 nm for 30 keV Ga<sup>+</sup> in Au) forcing the whole film to bend such as if it was a freestanding cantilever it will curl upwards and if it is clamped it will bow downwards.

Although the swelling/bending mechanisms are still unclear and somewhat contradictory, researchers have been using ion implantation to bend cantilevers for micro-mechanical applications [48, 49] or producing kirigami structures for optimal chirality control [47]. These experiments show that low-dose implantations can cause a change in the in-plane dimensions which in turn translates into an out-of-plane swelling and/or suspended thin-film buckling.

Thus, while these investigations have made significant strides in clarifying the complexities of shape manipulation through ion implantation, it is worth noting that the studies have primarily concentrated on scrutinizing the ion-implanted region, overlooking the examination of the adjacent unexposed area. Here, we highlight that induced strain through ion implantation (and damage) could be utilized to generate strains, thereby altering the band structure of semiconductors in the adjacent pristine and crystalline regions. Thus, despite the efficacy of the implantation techniques in regulating the morphology of membranes and cantilevers, it is an oversight not to analyze the neighboring unexposed region.

### 3. Recent advances

This perspective article explores a specific strategy to overcome the optical fundamental barrier that constrains the global application of group-IV semiconductors as active optoelectronic structures. Specifically, we examine the potential of a novel material-engineering approach aimed at realizing high optical efficiency devices on group-IV semiconductors while also addressing the associated challenges. Masteghin *et al* [50] showed that it is possible, in principle, to achieve an indirect-to-direct bandgap transition in suspended single-crystal semiconductors through a scalable single-step approach employing ion implantation—an established technique within the semiconductor industry. The authors have demonstrated a single-step procedure that controllably produced, in single-crystal silicon membranes, record high tensile strains, both biaxial (up to 3.1%) and uniaxial (up to 8.5%). These strains were achieved using direct-write focused ion beam (FIB) implantation around the active membrane regions. This route offers the tantalizing prospect of being able to develop direct bandgap group-IV materials that may be further functionalized for use in photonic devices, e.g. through the development of highly confined photonic crystals or nano-cavity-based lasers. These single-crystal Si membranes were commercially produced by back-etching a SOI wafer having a 35 nm thick device layer. The membrane window dimensions are defined by the opening (exposed Si area) on the wafer's backside and the wafer thickness, based on the Si etch angle of 54.7° under anisotropic potassium hydroxide (KOH) etching [51–53]. The window edges and diagonals are typically oriented along the <110> and <100> directions, respectively. When a buffer layer is present, hydrofluoric acid (HF) is used to etch the silicon dioxide (SiO<sub>2</sub>) [54]. Production processes may vary but usually involve thinning the active layer via reactive ion etching [55], photolithography to expose specific regions on the backside, and sputtering or evaporation of etchant-resistant layers (e.g. silicon nitride). Similar procedures

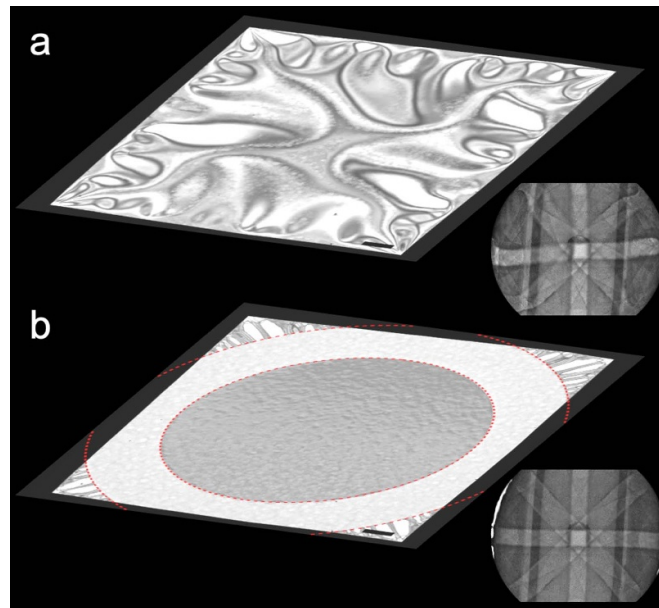


**Figure 2.** Flattening of a buckled single-crystal silicon membrane prepared by back-etching a SOI wafer. The 35 nm thick device layer buckles due to unintentional compressive forces that arise due to reasons mentioned in section 2.1. (a) 30 keV bright-field scanning transmission electron microscopy (BF-STEM) image of the pristine membrane, in which the observed contrast is due to electron channeling probability. The STEM detector subset counts are subjected to curvature-induced scattering, e.g., when imaging in BF mode the flattest region will appear brighter—no curvature, hence more detection events at the beam axis. (b) BF-STEM micrograph of the membrane following  $\text{Xe}^+$  ion implantation ( $8.7 \times 10^{14}$  ions  $\text{cm}^{-2}$ ) into the region delimited by the red-dashed lines. In (b), the contrast alludes to a flat implanted ( $20 \mu\text{m}$  wide annulus) and tensioned region  $100 \mu\text{m}$  diameter circle surrounded by the implanted region, though presenting thickness dissimilarity from sputtering events during implantation. The diffraction patterns were collected from a probed region  $\sim 0.01 \text{ mm}$  wide at the center of the membrane window and show an improvement of the long-range order following the flattening experiment. Reprinted (figure) with permission from [50], Copyright (2021) by the American Physical Society.

can be applied to doped Si wafers, with a few exceptions to the steps required when starting from SOI.

Figure 2 shows an example of a silicon membrane before (figure 2(a)) and after (figure 2(b)) implantation within the region demarcated by the red dashed annulus. The membrane is initially wrinkled due to slight compression, while after treatment the membrane is very flat. The technique generates compression of the implanted annular region, referred to as the tensioner (marked within red-dashed lines in figure 2(b)), and this causes in-plane tension in the neighboring crystalline part, the central disk named the tympanum, like tightening a drum skin. The amount of stress produced by the tensioner is controlled by the ion dosage (in  $\text{cm}^{-2}$ ) and its geometry. The ion implantation process allows the (non-implanted) tympanum region of the membrane to go from its initial compressive state to a tensile strain (passing, obviously, through an unstrained state). The whole process takes only 74 s using a 30 keV  $\text{Xe}^+$  beam with 150 pA current to implant an area of  $0.008 \text{ mm}^2$  and to strain an area of similar size. The wrinkle reduction (flattening) is highlighted by the improvement of the long-range order in the Kikuchi bands (figure 2) obtained by rocking the electron beam concentric to a point at the center of the membrane, with a probing area estimated to be around  $10 \mu\text{m}$  in diameter. Here, it is worth mentioning that the flattening of suspended single-crystal thin films is an important accomplishment itself since many diffraction-based techniques require a lower background signal (lack of bulk material under the modified surface) with a consistent Bragg-angle or zone-axis position throughout the scanned area.



A high angular resolution electron backscatter diffraction (HR-EBSD) map of an even smaller circular tympanum (higher strain) displayed negligible out-of-plane rotation at the center, with a curvature equals to  $0.2^\circ \mu\text{m}^{-1}$  at its circumference [50]. The somewhat concave shape of the tympanum suggests a downward bowing of the adjoining tensioner, resulting from being contracted whilst clamped on both sides (i.e. by the bulk Si frame and the crystalline part of the membrane). The confirmation of induced compression on the top surface (in ion range) of the implanted region came from observing the upward curling in thin cantilevers [50]. These cantilever-like structures were cut from the membrane using conventional FIB milling followed by ion implantation under similar conditions from the flattening experiment.

The authors [50], quantified the tympana strain via micro-Raman spectroscopy, which is an indirect technique. Shifts in the silicon  $T_{2g}$  mode at  $\omega_0 = 521 \text{ cm}^{-1}$  are expected following variations in the crystal lattice caused by strain. The magnitude of the induced strain can be related to the peak shift ( $\Delta\omega$ , in  $\text{cm}^{-1}$ ) based on [56]:

$$\Delta\omega (\text{cm}^{-1}) = \frac{1}{2\omega_0} [pS_{12} + q(S_{11} + S_{12})] \sigma, \quad (1)$$

being  $\sigma$  the stress (in Pa),  $p$  and  $q$  material's constants, and  $S_{ij}$  silicon compliance tensor elements. Using reported values [56] of  $p = -1.43\omega_0^2$ ,  $q = -1.89\omega_0^2$ ,  $S_{11} = 7.68 \times 10^{-2} \text{ Pa}^{-1}$ , and  $S_{12} = -2.14 \times 10^{-12} \text{ Pa}^{-1}$ , equation (1) becomes:

$$\sigma (\text{Pa}) = \frac{\Delta\omega (\text{cm}^{-1})}{-2 \times 10^{-9}}, \quad (2)$$

$$\frac{(\sigma_{xx} + \sigma_{yy})}{2} (\text{Pa}) = \frac{\Delta\omega (\text{cm}^{-1})}{-4 \times 10^{-9}}, \quad (3)$$

being equation (2) for uniaxial stress and equation (3) for in-plane biaxial stress. Based on equations (2) and (3) above, for Raman equipment that is able to detect shifts of  $0.02 \text{ cm}^{-1}$ , an uniaxial stress of 10 MPa or biaxial stress of 5 MPa can be detected. Using the appropriate Young's modulus for silicon—such as 180 GPa for biaxial stress or 130 GPa and 169 GPa for the  $\langle 100 \rangle$  and  $\langle 110 \rangle$  directions [57], this technique could theoretically detect minimum strain values as low as 0.003%. For instance, Englert *et al* [58] observed a redshift of  $\Delta\omega = 2.8 \text{ cm}^{-1}$ , which based on equation (3) corresponds to a tensile stress of 700 MPa. Here, we note that several conversion coefficients are available in the literature [56, 59–63]. However, in the work of Masteghin *et al* [50], which will be the focus of this perspective article, conservative literature values [60] of phonon deformation potentials were used when extracting strain values based on shifts in the micro-Raman  $T_{2g}$  mode. This approach resulted in reported strains up to 15% smaller than those that would be obtained using recent conversion values.

In the work [50], the shift in the  $521 \text{ cm}^{-1}$  Raman line was calibrated against the known variation with strain to estimate in-plane tensile strain in single-crystal Si membranes. It is known that this technique can suffer from artifacts, such as laser-induced thermal shifts unrelated to the induced strain [64, 65]. The redshifts caused by laser light absorption (i.e. heating) are primarily a consequence of crystal expansion, where an increase in the lattice parameters reduces the vibrational frequencies of the phonons, similar to the effects of strain. Additionally, anharmonic coupling mechanisms at higher temperatures can further contribute to changes in phonon frequencies [66, 67]. To mitigate such problems, the 532 nm laser power was reduced below the point where power-dependent Raman shifts could be detected (aided by in-line optical filters, reaching  $\sim 100 \mu\text{W} \mu\text{m}^{-2}$ ). Short acquisition times were also used. Several other tests were used to confirm that the Raman shifts are strain-related rather than

laser-power-related. During the uniaxial straining tests, the rectangular tympana (non-exposed regions) had their shorter length oriented along different silicon crystal directions, such as [010], [110], and [120], followed by redshifts that followed just what one would expect based on the anisotropic values for Young's modulus. The less stiff  $\langle 010 \rangle$  direction allowed for an enhanced bowing of the tensioner region, which, in turn, resulted in a higher outward pulling force at the center of the tympanum. However, since thermal conductivity in Si does not depend on the crystal orientation, such intense redshifts would not be observed if laser-induced heating was the main mechanism responsible for shifts in the  $T_{2g}$  peak. In addition, another test was carried out in which a tensioner was implanted around an 8  $\mu\text{m}$  diameter tympanum, creating a top amorphous Si layer whose thickness has been defined by the ion distribution profile. The membrane had its tensioner implanted again from the opposite side (turning the sample upside-down), ensuring that the whole tensioner volume was amorphous. As a result, there was a restoration of the  $T_{2g}$  peak shift back towards equilibrium (i.e. it was still red-shifted compared to bulk unstrained Si but blue-shifted compared to the first spectrum acquired at the center of the tympanum). If thermal effects were responsible for the Raman shift it would be expected that the back-side implantation would induce further redshifts since amorphous Si has a thermal conductivity one hundred times lower than crystalline Si [68]. Secondly, this also shows that the bilayer structure formed by a top amorphous layer and an underlying crystalline layer plays a key role in generating strain, and this bilayer structure is eliminated when both sides of the membrane tensioner are implanted. The strain, apparently, is not simply due to the contraction of the amorphized layer(s), and the presence of the crystalline part is required. This implies that the interface between the crystalline part and the amorphized layer of the structure is important in some still unknown way.

The microscopic mechanisms for the generation of the strain were explored using single-side exposure on simpler cantilever-like structures. After observing the bending in such cantilevers following implants at different acceleration energies, the authors [50] opted to use a bilayer structure model to elucidate the ion beam-induced strain mechanism. Building on the classic Timoshenko's theory [69], the authors derived a simplified model to explain the measured cantilevers' curvature following  $\text{Ga}^+$  irradiation [50]. The approximation shows that the radius of curvature  $R$  for a free-standing bilayer is minimized when the layers have equal thickness and equal Young's modulus, in which case  $R = 2t/3\Delta$  (see supplementary material of [50] for the full derivation) where  $t$  is the total thickness and  $\Delta = (L_1 - L_2)/L_2$  is the relative difference in the natural lengths of the layers, i.e. the induced misfit strain. This model explains why cantilever curvature was optimal when the ion implantation was tuned to amorphize only half of the membrane thickness at low fluence and dosage in the top implanted layer. However, the typical radius of curvature was a few microns for a film of thickness a few tens of nm, meaning the misfit strain in the tensioner from the Timoshenko model was only on the order of 1%. Based on that, geometric amplification by a large area of tensioner with a small area of tympanum was used to explain the large induced strains observed. Though, several questions remain open regarding the mechanics involved in this complex system:

- (i) How does the implantation/amorphization of the top layer induce sufficient tensile stress on the neighboring tympanum? Is the induced misfit strain in the implanted layer sufficient to explain the observed tympanum strain?
- (ii) Could the boundary between amorphous and crystalline Si be an enhancing factor required to generate the strain observed? Might lateral forces be induced in the crystalline part where it is in contact with the amorphized layer due to the reconstruction of broken bonds, just as Si does at free surfaces?

A high-resolution strain mapping would be ideal to try to elucidate the mechanisms involved and to report a direct measurement of strain distribution across the tympanum. However, techniques are limited and consist of either 4D-scanning transmission electron microscopy (4D-STEM) or synchrotron nano-x-ray diffraction (nano-XRD). Advantages of 4D-STEM for strain mapping include ultra-high spatial resolution and lack of background signal but, similarly to EBSD, it can only report relative strain concerning a region deemed as reference. Therefore, absolute strain value measurements would still not be possible. On the other hand, synchrotron nano-XRD provides a route to determine absolute strain values following a calibration that does not need to be performed close to the region of interest. Nonetheless, such a technique comes with its costs such as difficult access to facilities, a much larger spot size (hence, lower spatial resolution), and the main issue, the background noise from the membrane frame. For this technique, the sample must be tilted to an angle ' $\theta$ ' in which the incident beam satisfies the Bragg condition, causing the incident beam to propagate and scatter through the bulk part of the membrane support, generating a strong diffraction signal compared to that from the 35 nm thick crystalline membrane. For lower strain values (small peak shift), the strong background signal is sufficient to prevent peak deconvolution. Ways to overcome the limitations mentioned when trying to obtain absolute strain values in such a system would be very valuable. We suggest some possible directions of future research that might help in this regard:

- (i) The use of precession electron diffraction in a 4D-STEM. This technique can reduce artifacts such as variations in membrane thickness or zone-axis misorientation caused by membrane buckling, including the inevitable transverse buckling controlled by Poisson's ratio; but using membranes that are partly covered by ultra-thin gold (Au) islands before the ion-implantation-induced strain. These Au islands can be formed after the thermal annealing of evaporated <10 nm Au films [70] as a result of the weak adhesion of thin Au on Si [71]. We believe that the gold islands will not be strained together with the tympanum since they are not directly connected to the tensioner, hence their constant (and well-characterized) lattice spacing values can be used as a camera length calibration specimen to measure absolute strain in the tympanum region. Although the intention is that the Au nanoparticles are weak perturbations, their non-invasiveness would need to be verified.
- (ii) Synchrotron nano-XRD measurements would have to be performed on membranes with a much larger area or much better focus so that fewer scattered photons penetrate the bulk region before scattering to populate the diffraction detector.

However, for both techniques (as with micro-Raman spectroscopy [72]), the probing depth is significantly greater than the membrane thickness. Without a method to profile the strain across the tympanum/tensioner thickness, our understanding of ion beam-induced strain in suspended single-crystal membranes remains limited.

The results described above and in figure 2 are for silicon. It is also paramount to transfer this methodology to Ge to achieve the highly desirable indirect-to-direct transition. But, as mentioned, firstly, it is essential to obtain high-quality Ge membranes, which is a bottleneck for scientific advancements in group-IV photonics. The easiest way to overcome this—and to allow large-scale production with higher reliability after integration—would be to modify the ion implantation methodology to induce strain in thicker membranes (with lower TDD at the surface). Based on the Timoshenko approximation, this would require higher implantation energies beyond the limits of conventional FIBs. While the reported approach uses a FIB for simplicity and quicker sample turnaround, it

could utilize lithographic processes (e.g. masked photolithography or electron beam lithography) and conventional broad-beam ion implantation to try inducing the contraction/bowing at the tensioner region and, consequently, strain the tympanum area. It is not presently clear if there is any fundamental difference between scanning FIB-induced strain technique and broad area. It may be that a small implantation spot size is required in which each implantation event causes a small localized contraction/bowing that when performed line-by-line results in an amplified curling phenomenon akin to the curling of ribbons [73] created by several nanometer-sized ‘blades’ at the point of each line scan (i.e.  $\sim 10$  nm apart from each other). It may be that a combination of broad-beam implantation with Sn-doped membranes produces an optimum straining effect. The membrane thickness dependence also needs investigation. For thin layers, one approach is to epitaxially grow thicker Ge epilayers. These can then be thinned down from the backside using KOH etching and/or reactive ion etching, leaving only the top tens of nanometers, which have a lower defect density compared to the interfacial region [33]. Of course, thin films limit the volume of the medium and therefore also the available light output.

Lastly, we would like to underscore that the employed technique [50] was systematically applied to Si membranes derived from both Si-on-Si and SOI wafers. The observations indicate a distinct variation in the threshold for flattening and straining rates based on the different initial stress states. Notably, and somewhat surprising, it has been found that membranes subjected to a compressive initial state exhibited a more efficient response, achieving a specified strain level at significantly lower ion dosage compared to other stress states. While the system can be readily calibrated for comprehensive quality control, understanding the underlying behavior requires elucidation through the development of bending models, a task that falls outside the scope of the current study.

In summary, there are still several open questions that must be answered before being able to achieve strained germanium light emitters based on this technique. First among these should be an elucidation of the strain generation mechanism and the manufacturing of high-quality sub-50 nm Ge membranes.

#### **4. Planning ahead: how can strain control in Si assist with qubit addressing?**

Although in 1998 Kane proposed a silicon-based quantum computer using the nuclear spin of donor impurities [74], the first commercial quantum computers (such as IBM Q System One) [75] have been based on other technologies such as superconducting resonators. The delay in the production of Kane’s qubit device stems from its design intricacies, notably the challenge of precisely positioning two phosphorus (P) ions apart from each other by 20 nm as well as 25 nm under the SiO<sub>2</sub> surface. Achieving the required level of precision for qubit separation is paramount to engineer the desired interaction between them for entangling gates. The positional accuracy of impurities is particularly crucial in Si due to the multivalley nature of its conduction band [76, 77]. Even slight variations in dopant separation can influence donor–donor exchange coupling, based on the destructive interference patterns generated by oscillations of donor wavefunctions at the lattice scale [78]. For instance, the Kohn–Luttinger effective mass approximation model predicts a variation in exchange splitting for Si:P donors of approximately 30 meV for a 0.4 nm separation along the [110] axis, starting from an initial P–P distance of about 7.3 nm [79].

This characteristic of Si makes manufacturing imperfections fundamentally overwhelming. However, the oscillatory dependence of the exchange splitting can be mitigated by applying strain of the appropriate sign and strength in the [110]

crystal direction [80]. By breaking the tetrahedral symmetry of the Si crystal through uniaxial strain, the degeneracy of valleys is lifted, and the ground states no longer oscillate with distance in the plane perpendicular to the strain direction [80]. With the correct uniaxial strain, the exchange splitting begins to decay monotonically. However, it continues to oscillate if there is positional inaccuracy in the [001] direction, which remains as oscillatory as before. Nonetheless, a potential solution lies in achieving an indirect-to-direct transition in either a Si or Ge host. This transition would reduce the number of valleys involved in producing the interference—ideally down to one—for all exchange coupling directions. Overall, even small strains can be beneficial for qubit operation since they change the valley character [81] or allow tuning of the electron spin resonance [82].

Photons can be used to address spin states in Si donors, but their detection has primarily been performed electrically [83, 84], which poses challenges due to the complex and small-scale lithography processes required. However, employing a direct bandgap host material can significantly enhance photon collection efficiency [85]. While this indirect-to-direct transition in Si and/or Ge has not yet been achieved, other approaches have been explored. For example, Loippo *et al* [86] investigate an indirect optical transition to address the bound exciton transition and probe its decay via changes in conductivity. Their work highlights the challenges of addressing bound excitons in P-donor spin in Si when employing a hybrid electro-optical readout technique. In particular, intrinsic strain, exacerbated by electrical contacts near the implanted region, complicates transition analysis and hinders the selective addressing of polarization-dependent exciton transitions. Considering these addressability challenges in P-donors in Si, the strain control technique developed by Masteghin *et al* [50] becomes pivotal. This methodology allows for precise control of strain in suspended single-crystal systems, enabling a seamless transition from compressive to highly tensile strained states as well as the ability to fully annihilate intrinsic strains.

Lastly, we would like to mention the work of Ristori *et al* [87] which reports the use of strain engineering to tune the splitting of the zero-phonon-line (ZPL) in G-centers. Their strained G-centers were produced in an 8-step procedure involving the implantation of carbon (C) ions followed by annealing; as well as proton ( $H^+$ ) implantation, photolithography, plasma etching, silicon nitride deposition (straining agent), etc. Again, this is a prime example that could benefit from the FIB-induced straining technique. Using a dedicated duoplasmatron FIB/single ion implanter [88], nearly all steps required for the creation of strained G-centers can be performed in a high-vacuum microscope chamber, except for annealing. This one-of-a-kind FIB allows one to deterministically implant  $C^+$  and  $H^+$ , and then irradiate the neighboring regions with  $Xe^+$  to induce tensile strain in the active region. These implantation events can occur without moving the sample, simply by exchanging the gas source, e.g. from an argon/carbon monoxide or argon/hydrogen to xenon. Therefore, the FIB-based methodology offers several advantages. It not only reduces processing time but also has the potential to increase production yield via increased control of impurities positioning. Furthermore, it enables better control over strain uniformity, which may lead to improvements in polarization degrees and ZPL linewidth.

Thus, the ion beam-induced strain technique holds promise for achieving several sought-after goals in both photonics and quantum technologies fields, offering multiple potential breakthroughs in these domains.

## 5. Closing remarks

In this Perspective, we discussed the advancements and prospects of a technique able to generate or annihilate (i.e. to control) strain in suspended thin films. While the primary focus revolves around this innovative application of FIBs, it is

imperative to underscore their versatility. Beyond their role as structural sculpting instruments, FIBs must also be recognized as transformative materials modification tools that could influence the trajectory of telecommunication and quantum technologies. FIBs could be instrumental in the fabrication of direct bandgap group-IV semiconductors discussed above, and they could also be used as the tool for deterministic implantation of impurity and color center spin qubits at the million scale. Being substrate agnostic, they could be used for solids and insulators, isotopically pure or natural composition substrates. The resulting control over the position, the number, and the local strain environment makes many new quantum technologies possible. As we reflect on these opportunities, it becomes evident that FIBs hold the potential not only to analyze but also to shape and advance the frontiers of materials science.

### Data availability statement

The data that support the findings of this study are openly available at the following URL/DOI: <https://10.5281/zenodo.10711907> [89].







### Acknowledgments

M G M and S K C acknowledge financial support from the Engineering and Physical Sciences Research Council (EPSRC) (Grant No. EP/X018989/1). M G M and S J S acknowledge financial support from EPSRC (Grant No. EP/V048732/1). ATI and IBC-based authors acknowledge financial support from EPSRC (Grant No. EP/W027070/1 and Grant No. EP/X015491/1). The authors thank Silson Ltd for their support.

### Funding

Engineering and Physical Sciences Research Council (EPSRC), Grant Nos. EP/X018989/1, EP/V048732/1, EP/W027070/1, and EP/X015491/1.

### ORCID iDs

Mateus G Masteghin  <https://orcid.org/0000-0002-5672-8311>  
Benedict N Murrin  <https://orcid.org/0000-0001-9219-652X>  
Dominic A Duffy  <https://orcid.org/0000-0002-7853-5107>  
Steven K Clowes  <https://orcid.org/0000-0003-3918-0080>  
David C Cox  <https://orcid.org/0000-0003-3742-9188>  
Stephen J Sweeney  <https://orcid.org/0000-0001-8561-6071>  
Roger P Webb  <https://orcid.org/0000-0002-9557-5207>

### References

- [1] Soref R 1998 Applications of silicon-based optoelectronics *MRS Bull.* **23** 20–24
- [2] Han Y, Park H, Bowers J and Lau K M 2022 Recent advances in light sources on silicon *Adv. Opt. Photonics* **14** 404–54
- [3] Xiang C, Jin W, Huang D, Tran M A, Guo J, Wan Y, Xie W, Kurczveil G, Netherton A M and Liang D 2021 High-performance silicon photonics using heterogeneous integration *IEEE J. Sel. Top. Quantum Electron.* **28** 1–15
- [4] Liu A Y, Srinivasan S, Norman J, Gossard A C and Bowers J E 2015 Quantum dot lasers for silicon photonics *Photon. Res.* **3** B1–9
- [5] Fitch C R, Baltušis A, Marko I P, Jung D, Norman J C, Bowers J E and Sweeney S J 2021 Carrier recombination properties of low-threshold 1.3  $\mu\text{m}$  quantum dot lasers on silicon *IEEE J. Sel. Top. Quantum Electron.* **28** 1–10

- [6] Moutanabbir O, Assali S, Gong X, O'Reilly E, Broderick C A, Marzban B, Witzens J, Du W, Yu S-Q and Chelnokov A 2021 Monolithic infrared silicon photonics: the rise of (Si) GeSn semiconductors *Appl. Phys. Lett.* **118** 110502
- [7] Armand Pilon F T, Lyasota A, Niquet Y-M, Reboud V, Calvo V, Pauc N, Widiez J, Bonzon C, Hartmann J-M, Chelnokov A, Faist J and Sigg H 2019 Lasing in strained germanium microbridges *Nat. Commun.* **10** 2724
- [8] Cheng S-L, Lu J, Shambat G, Yu H-Y, Saraswat K, Vuckovic J and Nishi Y 2009 Room temperature 1.6  $\mu\text{m}$  electroluminescence from Ge light emitting diode on Si substrate *Opt. Express* **17** 10019–24
- [9] Castellano A, Cerutti L, Rodriguez J B, Narcy G, Garreau A, Lelarge F and Tournié E 2017 Room-temperature continuous-wave operation in the telecom wavelength range of GaSb-based lasers monolithically grown on Si *APL Photonics* **2** 061301
- [10] Fischetti M V and Laux S E 1996 Band structure, deformation potentials, and carrier mobility in strained Si, Ge, and SiGe alloys *J. Appl. Phys.* **80** 2234–52
- [11] Vogl P, Rieger M M, Majewski J A and Abstreiter G 1993 How to convert group-IV semiconductors into light emitters *Phys. Scr.* **1993** 476
- [12] Kúsová K, Hapala P, Valenta J, Jelínek P, Cibulka O, Ondič L and Pelant I 2014 Direct bandgap silicon: tensile-strained silicon nanocrystals *Adv. Mater. Interfaces* **1** 1300042
- [13] Li S, Chou J-P, Zhang H, Lu Y and Hu A 2019 A study of strain-induced indirect-direct bandgap transition for silicon nanowire applications *J. Appl. Phys.* **125** 082520
- [14] Sweeney S J, Eales T D and Adams A R 2019 The impact of strained layers on current and emerging semiconductor laser systems *J. Appl. Phys.* **125** 082538
- [15] Schaller R R 1997 Moore's law: past, present and future *IEEE Spectr.* **34** 52–59
- [16] Lundstrom M 2003 Moore's law forever? *Science* **299** 210–1
- [17] Thompson S E and Parthasarathy S 2006 Moore's law: the future of Si microelectronics *Mater. Today* **9** 20–25
- [18] Joyce H J, Parkinson P, Jiang N, Docherty C J, Gao Q, Tan H H, Jagadish C, Herz L M and Johnston M B 2014 Electron mobilities approaching bulk limits in "surface-free" GaAs nanowires *Nano Lett.* **14** 5989–94
- [19] Uchida K, Kinoshita A and Saitoh M 2006 Carrier transport in (110) nMOSFETs: subband structures, non-parabolicity, mobility characteristics, and uniaxial stress engineering 2006 *Int. Electron Devices Meeting (IEEE)* pp 1–3
- [20] Lee W, Hwangbo Y, Kim J-H and Ahn J-H 2016 Mobility enhancement of strained Si transistors by transfer printing on plastic substrates *npj Asia Mater.* **8** e256
- [21] Paul D J 2004 Si/SiGe heterostructures: from material and physics to devices and circuits *Semicond. Sci. Technol.* **19** R75
- [22] Whall T E and Parker E H C 2000 SiGe-heterostructures for CMOS technology *Thin Solid Films* **367** 250–9
- [23] Krijn M 1991 Heterojunction band offsets and effective masses in III–V quaternary alloys *Semicond. Sci. Technol.* **6** 27
- [24] Rainko D, Ikonic Z, Vukmirović N, Stange D, von den Driesch N, Grützmacher D and Buca D 2018 Investigation of carrier confinement in direct bandgap GeSn/SiGeSn 2D and 0D heterostructures *Sci. Rep.* **8** 15557
- [25] Wirths S, Geiger R, von den Driesch N, Mussler G, Stoica T, Mantl S, Ikonic Z, Luysberg M, Chiussi S and Hartmann J-M 2015 Lasing in direct-bandgap GeSn alloy grown on Si *Nat. Photon.* **9** 88–92
- [26] Eales T D, Marko I P, Schulz S, O'Halloran E, Ghetmiri S, Du W, Zhou Y, Yu S-Q, Margetis J, Tolle J, O'Reilly E P and Sweeney S J 2019 Ge<sub>1-x</sub>Sn<sub>x</sub> alloys: consequences of band mixing effects for the evolution of the band gap  $\Gamma$ -character with Sn concentration *Sci. Rep.* **9** 14077
- [27] Koerner R, Oehme M, Gollhofer M, Schmid M, Kostecki K, Bechler S, Widmann D, Kasper E and Schulze J 2015 Electrically pumped lasing from Ge Fabry-Perot resonators on Si *Opt. Express* **23** 14815–22
- [28] Mirbaha S and Tait R N 2010 Metal-semiconductor-metal photodetector with a-Ge: h absorption layer for 1.55  $\mu\text{m}$  optical communication wavelength *Proc. SPIE* **7750** 474–9
- [29] LeGoues F K, Copel M and Tromp R 1989 Novel strain-induced defect in thin molecular-beam epitaxy layers *Phys. Rev. Lett.* **63** 1826
- [30] Eaglesham D J and Cerullo M 1991 Low-temperature growth of Ge on Si (100) *Appl. Phys. Lett.* **58** 2276–8
- [31] Hantschmann C, Liu Z, Tang M, Chen S, Seeds A J, Liu H, White I H and Pentz R V 2020 Theoretical study on the effects of dislocations in monolithic III–V lasers on silicon *J. Lightwave Technol.* **38** 4801–7
- [32] Camassel J and Tiberj A 2003 Strain effects in device processing of silicon-on-insulator materials *Appl. Surf. Sci.* **212** 742–8
- [33] Yu X, Jia H, Yang J, Masteghin M G, Beere H, Mtunzi M, Deng H, Huo S, Chen C, Chen S, Tang M, Sweeney S J, Ritchie D, Seeds A and Liu H 2024 Effects of phosphorous and antimony doping on thin Ge layers grown on Si *Sci. Rep.* **14** 7969
- [34] Burt D, Al-Attili A, Li Z, Gardès F, Sotto M, Higashitarumizu N, Ishikawa Y, Oda K, Querin O M, Saito S and Kelsall R 2017 Enhanced light emission from improved

- homogeneity in biaxially suspended Germanium membranes from curvature optimization *Opt. Express* **25** 22911–22
- [35] Minamisawa R A, Süess M J, Spolenak R, Faist J, David C, Gobrecht J, Bourdelle K K and Sigg H 2012 Top-down fabricated silicon nanowires under tensile elastic strain up to 4.5% *Nat. Commun.* **3** 1096
- [36] Backman M 2012 Effects of nuclear and electronic stopping power on ion irradiation of silicon-based compounds
- [37] Ziegler J F, Ziegler M D and Biersack J P 2010 SRIM—The stopping and range of ions in matter *Nucl. Instrum. Methods Phys. Res. B* **268** 1818–23
- [38] Cox D C 2015 Focused ion beam. *Introduction to Focused Ion Beam Nanometrology*
- [39] Rymzhanov R A, Gorbunov S A, Medvedev N and Volkov A E 2019 Damage along swift heavy ion trajectory *Nucl. Instrum. Methods Phys. Res. B* **440** 25–35
- [40] Schenkel T, Hamza A V, Barnes A V and Schneider D H 1999 Interaction of slow, very highly charged ions with surfaces *Prog. Surf. Sci.* **61** 23–84
- [41] Kim Y-R, Chen P, Aziz M J, Branton D and Vlassak J J 2006 Focused ion beam induced deflections of freestanding thin films *J. Appl. Phys.* **100** 104322
- [42] Grimvall G 1999 Elasticity. Basic relations *Thermophysical Properties of Materials G Grimvall* (Elsevier Science B.V.) pp 27–45
- [43] Van Dillen T, Polman A, Fukarek W and Van Blaaderen A 2001 Energy-dependent anisotropic deformation of colloidal silica particles under MeV Au irradiation *Appl. Phys. Lett.* **78** 910–2
- [44] Benyagoub A, Löffler S, Rammensee M, Klaumünzer S and Saemann-Ischenko G 1992 Plastic deformation in SiO<sub>2</sub> induced by heavy-ion irradiation *Nucl. Instrum. Methods Phys. Res. B* **65** 228–31
- [45] Frey L, Lehrer C and Ryssel H 2003 Nanoscale effects in focused ion beam processing *Appl. Phys. A* **76** 1017–23
- [46] Chee S W, Kammler M, Graham J, Gignac L, Reuter M C, Hull R and Ross F M 2018 Directed self-assembly of Ge quantum dots using focused Si<sup>2+</sup> Ion beam patterning *Sci. Rep.* **8** 9361
- [47] Liu Z, Du H, Li J, Lu L, Li Z-Y and Fang N X 2018 Nano-kirigami with giant optical chirality *Sci. Adv.* **4** eaat4436
- [48] Arora W J, Smith H I and Barbastathis G 2007 Membrane folding by ion implantation induced stress to fabricate three-dimensional nanostructures *Microelectron. Eng.* **84** 1454–8
- [49] Salvati E, Sui T, Lunt A J G and Korsunsky A M 2016 The effect of eigenstrain induced by ion beam damage on the apparent strain relief in FIB-DIC residual stress evaluation *Mater. Des.* **92** 649–58
- [50] Masteghin M G, Tong V, Schneider E B, Underwood C C L, Peach T, Murdin B N, Webb R P, Clowes S K and Cox D C 2021 Stress-strain engineering of single-crystalline silicon membranes by ion implantation: towards direct-gap group-IV semiconductors *Phys. Rev. Mater.* **5** 124603
- [51] Palik E D, Glembocki O J and Stahlbush R E 1988 Fabrication and characterization of Si membranes *J. Electrochem. Soc.* **135** 3126
- [52] Vu Q, Stricker D A and Zavracky P M 1996 Surface characteristics of (100) silicon anisotropically etched in aqueous KOH *J. Electrochem. Soc.* **143** 1372
- [53] Zubei I 2000 Silicon anisotropic etching in alkaline solutions III: on the possibility of spatial structures forming in the course of Si (100) anisotropic etching in KOH and KOH + IPA solutions *Sens. Actuators A* **84** 116–25
- [54] Witvrouw A, Du Bois B, De Moor P, Verbist A, Van Hoof C A, Bender H and Baert C 2000 Comparison between wet HF etching and vapor HF etching for sacrificial oxide removal *Proc. SPIE* **4174** 130–41
- [55] Jansen H, Gardeniers H, de Boer M, Elwenspoek M and Fluitman J 1996 A survey on the reactive ion etching of silicon in microtechnology *J. Micromech. Microeng.* **6** 14
- [56] De Wolf I 1996 Micro-Raman spectroscopy to study local mechanical stress in silicon integrated circuits *Semicond Sci. Technol.* **11** 139
- [57] Hopcroft M A, Nix W D and Kenny T W 2010 What is the Young's Modulus of Silicon? *J. Microelectromech. Syst.* **19** 229–38
- [58] Englert T, Abstreiter G and Pontcharra J 1980 Determination of existing stress in silicon films on sapphire substrate using Raman spectroscopy *Solid-State Electron.* **23** 31–33
- [59] Cerdeira F, Buchenauer C J, Pollak F H and Cardona M 1972 Stress-induced shifts of first-order Raman frequencies of diamond-and zinc-blende-type semiconductors *Phys. Rev. B* **5** 580
- [60] Anastassakis E, Cantarero A and Cardona M 1990 Piezo-Raman measurements and anharmonic parameters in silicon and diamond *Phys. Rev. B* **41** 7529
- [61] Anastassakis E, Pinczuk A, Burstein E, Pollak F H and Cardona M 1993 Effect of static uniaxial stress on the Raman spectrum of silicon *Solid State Commun.* **88** 1053–8
- [62] Peng C-Y, Huang C-F, Fu Y-C, Yang Y-H, Lai C-Y, Chang S-T and Liu C W 2009 Comprehensive study of the Raman shifts of strained silicon and germanium *J. Appl. Phys.* **105** 083537



- [63] Ureña F, Olsen S H and Raskin J-P 2013 Raman measurements of uniaxial strain in silicon nanostructures *J. Appl. Phys.* **114** 144507
- [64] Nikolenko A S 2013 Laser heating effect on Raman spectra of Si nanocrystals embedded into SiO<sub>x</sub> matrix *Semicond. Phys., Quantum Electron. Optoelectron.* **16** 86–90
- [65] Suess M J, Minamisawa R A, Geiger R, Bourdelle K K, Sigg H and Spolenak R 2014 Power-dependent Raman analysis of highly strained Si nanobridges *Nano Lett.* **14** 1249–54
- [66] Hart T R, Aggarwal R L and Lax B 1970 Temperature dependence of Raman scattering in silicon *Phys. Rev. B* **1** 638
- [67] Burke H H and Herman I P 1993 Temperature dependence of Raman scattering in Ge<sub>1-x</sub>Si<sub>x</sub> alloys *Phys. Rev. B* **48** 15016
- [68] Wada H W H and Kamijoh T K T 1996 Thermal conductivity of amorphous silicon *Jpn. J. Appl. Phys.* **35** L648
- [69] Timoshenko S 1925 Analysis of bi-metal thermostats *J. Opt. Soc. Am.* **11** 233–55
- [70] Yan C, Chen Y, Jin A, Wang M, Kong X, Zhang X, Ju Y and Han L 2011 Molecule oxygen-driven shaping of gold islands under thermal annealing *Appl. Surf. Sci.* **258** 377–81
- [71] Bhattarai J K, Neupane D, Nepal B, Alharthi M D, Demchenko A V and Stine K J 2020 Adhesion layer-free attachment of gold on silicon wafer and its application in localized surface plasmon resonance-based biosensing *Sens. Actuators A* **312** 112155
- [72] Yoo W S, Kim J H and Han S M 2014 Multiwavelength Raman characterization of silicon stress near through-silicon vias and its inline monitoring applications *J. Micro/Nanolithogr. MEMS MOEMS* **13** 11205
- [73] Prior C, Moussou J, Chakrabarti B, Jensen O E and Juel A 2016 Ribbon curling via stress relaxation in thin polymer films *Proc. Natl Acad. Sci.* **113** 1719–24
- [74] Kane B E 1998 A silicon-based nuclear spin quantum computer *Nature* **393** 133–7
- [75] Silva V and Silva V 2018 Enter the IBM Q Experience: a One-of-a-Kind Platform for Quantum Computing in the Cloud *Practical Quantum Computing for Developers: Programming Quantum Rigs in the Cloud using Python, Quantum Assembly Language and IBM QExperience* pp 77–141
- [76] Ramdas A K and Rodriguez S 1981 Spectroscopy of the solid-state analogues of the hydrogen atom: donors and acceptors in semiconductors *Rep. Prog. Phys.* **44** 1297
- [77] Tankasala A, Salfi J, Bocquel J, Voisin B, Usman M, Klimeck G, Simmons M Y, Hollenberg L C L, Rogge S and Rahman R 2018 Two-electron states of a group-V donor in silicon from atomistic full configuration interactions *Phys. Rev. B* **97** 195301
- [78] Gamble J K, Jacobson N T, Nielsen E, Baczewski A D, Moussa J E, Montaño I and Muller R P 2015 Multivalley effective mass theory simulation of donors in silicon *Phys. Rev. B* **91** 235318
- [79] Pica G, Lovett B W, Bhatt R N and Lyon S A 2014 Exchange coupling between silicon donors: the crucial role of the central cell and mass anisotropy *Phys. Rev. B* **89** 235306
- [80] Wellard C J and Hollenberg L C L 2005 Donor electron wave functions for phosphorus in silicon: beyond effective-mass theory *Phys. Rev. B* **72** 085202
- [81] Voisin B, Ng K S H, Salfi J, Usman M, Wong J C, Tankasala A, Johnson B C, McCallum J C, Hutin L and Bertrand B 2022 Valley population of donor states in highly strained silicon *Mater. Quantum Technol.* **2** 025002
- [82] Mansir J, Conti P, Zeng Z, Pla J J, Bertet P, Swift M W, Van de Walle C G, Thewalt M L W, Sklenard B, Niquet Y-M and Morton J J L 2018 Linear hyperfine tuning of donor spins in silicon using hydrostatic strain *Phys. Rev. Lett.* **120** 167701
- [83] Yin C, Rancic M, de Boo G G, Stavrias N, McCallum J C, Sellars M J and Rogge S 2013 Optical addressing of an individual erbium ion in silicon *Nature* **497** 91–94
- [84] Higginbottom D B *et al* 2022 Optical observation of single spins in silicon *Nature* **607** 266–70
- [85] Chatterjee A, Stevenson P, De Franceschi S, Morello A, de Leon N P and Kuemmeth F 2021 Semiconductor qubits in practice *Nat. Rev. Phys.* **3** 157–77
- [86] Loippo T, Kannianen A and Muhonen J T 2023 Strain effects in phosphorus bound exciton transitions in silicon *Phys. Rev. Mater.* **7** 016202
- [87] Ristori A, Khoury M, Salvalaglio M, Filippatos A, Amato M, Herzig T, Meijer J, Pezzagna S, Hannani D, Bollani M, Barri C, Ruiz C M, Granchi N, Intonti F, Abbarchi M and Biccari F 2024 Strain engineering of the electronic states of silicon-based quantum emitters *Adv. Opt. Mater.* **12** 2301608
- [88] Cassidy N, Blenkinsopp P, Brown I, Curry R J, Murrin B N, Webb R and Cox D 2021 Single ion implantation of bismuth *Phys. Status Solidi A* **218** 2000237
- [89] Masteghin M G, Murrin B N, Duffy D A, Clowes S K, Cox D C, Sweeney S J and Webb R P 2024 *Advancements and challenges in strained group-IV-based optoelectronic materials stressed by ion beam treatment Zenodo* (<https://doi.org/10.5281/zenodo.10711907>)